RSC Advances

ROYAL SOCIETY OF CHEMISTRY

www.rsc.org/advances

Cite this: DOI: 10.1039/c0xx00000x

www.rsc.org/xxxxxx

ARTICLE TYPE

Topochemical synthesis of Bi_2O_3 microribbons derived from bismuth oxalate precursor as high-performance lithium-ion batteries†

Hai Wang, Hongxing Yang,* and Lin Lu

Received (in XXX, XXX) Xth XXXXXXXXX 20XX, Accepted Xth XXXXXXXXX 20XX

DOI: 10.1039/b000000x

Bismuth oxides (α-Bi_2O_3) microribbons are prepared from a precursor of $Bi(C_2H_4)OH$ (BICH) with ribbon shape. The as-prepared BICH is obtained through a facile hydrothermal procedure of the mixture of bismuth nitrate and oxalic acid aqueous solution. XRD, FESEM, TEM and TG-DTG are used to characterize the BICH. The obtained BICH precursor consists of one-dimensional crystal structure, and has a width of 1 to 2 μm, a thickness of 200 to 400 nm, and a length of 5 to 20 μm. The thermal decomposition of the BICH microribbons leads to the formation of well-defined Bi_2O_3 microribbons structure without morphology change. Compared to commercial Bi_2O_3 powder, the as-prepared Bi_2O_3 acted as anode of lithium-ion batteries (LIBs) shows a higher capacity of about 1047 mAh g^{-1} at 150 mA g^{-1} after 100th cycle. The good performance of the Bi_2O_3 microribbons can be attributed to better charge transfer properties, and shorter lithium-ion diffusion path. Owing to their excellent cyclability and rate performance, the Bi_2O_3 microribbons may become promising candidates for high-performance LIBs application in the future.

1. Introduction

Over the last decade, lithium-ion batteries (LIBs) have received considerable attention due to their wide range of applications, such as cell phones and hybrid vehicles.[1, 2] Among the increasing demands of LIBs performance, higher energy density, power density and more stable cycle performance are a prerequisite to the scientific consideration of practice application. Metal oxides, as one of the most promising candidates to graphite anode materials of LIBs, have been extensively carried out due to their high capacity, low cost and superior cycle performance.[3-6] Among these metal oxides anodes of LIBs, for example, TiO_2, SnO_2 have been the main research focus.[4, 7] Currently, the TiO_2, SnO_2 and their corresponding hierarchical nanostructured materials, nanocomposites, et al have been reported separately.[4, 5, 8-10] Simultaneously, great efforts have recently been devoted to exploring new electrode materials with new functionalities in academia and innovative industrial application. For example, element semiconductor Si and metal Sn were also widely studied.[11-14]

Drawing inspiration from the Sn and Si anode materials, Bi has been believed to act as an anode material for LIBs as well.[15, 16] Considering its quite high volumetric capacity (about 3765 mAh cm^{-3}), the bismuth based compounds, such as bismuth telluride, bismuth sulphide have been studied as novel anode materials of LIBs.[15-17] Very recently, Luo, et al reported that the direct growth of Bi_2O_3 on the surface Ni foam via a facile polymer-assisted solution approach and made an elegant comparative electrochemical analysis with commercial Bi_2O_3 powder.[18] These studies were interesting and meaningful works and, indeed, improved the capacity and stable performance obviously. From the point of view of microstructure of materials, their work main focused on the Bi_2O_3 nanocrystals. It is well-known that the anode materials morphology is an important feature for the development of high-performance LIBs. How to synthesis appropriate microstructure of materials is nowadays a hot topic. Previously, we demonstrated that TiO_2 anode materials with various hierarchical structures delivered superior electrochemical performance.[5, 9, 19] Therefore, exploring new Bi_2O_3 structure is both an extremely meaningful and imperative for LIB applications in the future.

According to the formula $t=L^2/D$, where L is the diffusion length, D is the diffusion coefficient for lithium ion and charge, the size of nanocrytals is an important factor for the improvement of LIBs performance, as shown in Scheme. 1. However, too small nanocrystals also would lead to some unexpected results thus caused poor cycling performance.[1-2] Currently, one-dimensional (1-D) nanostructures, for example, nanotubes, nanorods and nanowires, have been attracting much attention owing to their effective charge transfer capability, and potential applications in LIBs.[3, 20-23] Other shapes, particularly, ribbon-shaped structures with rectangular cross-sections, have been synthesized and used as LIBs anodes.[24-26] It is believed that the unique morphology of electrode materials is favourable for charge transfer and lithium ion diffusion owing to the high interfacial contact area between the electrodes and the electrolyte, and good mechanic accommodation of strain and volume change caused during

charge-discharge process. Therefore, the development of 1-D Bi_2O_3 ribbon-like structure with conductive layer is highly desired for high performance anode in practical LIBs.

Currently, Bi_2O_3 nanocrystals with irregular morphology have also been synthesized recently by a solution-based approach.[27, 28] However, to meet the demands of ribbon-like Bi_2O_3 anodes in LIBs, there are two prerequisites, one is stable material microstructure, the other is its conductivity. For former, it is difficult to synthesis due to the monoclinic crystal structure of Bi_2O_3; for latter, it is still great challenge for one-step solution process due to the limited approaches, although much efforts had been devoted to developing the carbon-coated techniques.

Herein, we first synthesized the bismuth oxalate precursor $Bi(C_2O_4)OH$ (BICH). The effect of hydrothermal reaction time on the formation of bisuth oxalates was investigated. It was found that the reaction time had an obvious effect on the dimensions of the precursor. Then the precursor was transformed into Bi_2O_3 microribbon via the simple thermal decomposition process. To the best of our knowledge, it is also a first report on the controlled dimensions of Bi_2O_3 with ribbon-like structure via the combination of chelation process and thermal decomposition. Most importantly, the amorphous carbon coated on the surface of the as-synthesized Bi_2O_3 microribbons was also obtained simultaneously during the thermal treatment. This method is completely different from the previously reported carbon-coated method, which may find new application in other transition metal oxides electrode materials, such as, Fe_3O_4, NiO, and et al. The Bi_2O_3 microribbons can deliver a capacity of about 1047 mAh g^{-1} after 100 cycles at 150 mAh g^{-1} and a stable capacity of 672 mAh g^{-1} even at a higher rate of 450 mAh g^{-1}.

2. Experimental section

2.1 Materials synthesis

Bismuth nitrate pentahydrate, anhydrous oxalic acid were of analytical grade and were used without further purification. In a typical procedure, 3 g of oxalic acid was dissolved in 60 mL DI water. After stirring for about 15 min, a transparent colorless aqueous solution was obtained. Then, 0.5 g of bismuth nitrate pentahydrate was slowly added the above solution. After stirring for about 30 min, the resulting solution was transferred into an autoclave and then sealed and heated at 170 ℃ for 14 h. After cooling down to room temperature, the as-formed precipitate was harvested by filtration and was washed several times with DI water and ethanol before it was dried in an vacuum oven at 80 °C for 2 h. The as-prepared Bi_2O_3 (denoted as A-Bi_2O_3) was obtained via thermal decomposition of BICH at 300 ℃ for 1 h. The electrochemical properties of A-Bi_2O_3 was further investigated and compared to commercial Bi_2O_3 powder (denoted as C-Bi_2O_3).

2.2 Material characterizations

The crystal phase was carried out by X-ray diffraction (XRD) analysis with a PANanalytic X'Pert spectrometer using Cu K_α radiation, λ=0.15405 nm. The morphologies of the as-made samples were observed on field-emission scanning electron microscope (JEOL JSM-7000F, Japan). The high-resolution transmission electron microscopy (HRTEM) images were obtained with a JEOL JEM-2010F microscopy operating at 200 Kv equipped with an energy dispersive X-ray spectrometry (EDX). The thermal decomposition behaviour of BICH microribbons was analysed by NETZSCH TG 209F1 Iris in N_2 atmosphere, Pt crucible, temperature range 30-800 °C (10 °C/min).

2.3 Electrochemical Measurements

The Bi_2O_3 electrodes were fabricated by spreading a mixture of 75 wt% Bi_2O_3 active material, 15 wt% a conductive agent (carbon black, Super-P-Li), and 10 wt% polymer binder polyvinylidene difluoride, PVDF on to a aluminum foil current collector. The mass loading of active material on each anode was about 3 mg. The as-made anodes were dried at 80 ℃ in vacuum oven for 24 h and pressed under 8 MPa. The electrodes were measured using coin cells (type CR2025) with pure lithium metal as both the counter electrode and the reference electrode at room temperature. Celgard 3400 membrane was used as a separator and 1.0 M $LiPF_6$ in a mixture of ethylene carbonate and diethyl carbonate (1: 1 volume, Novolyte Technologies, USA as the electrolyte). Cell assembly was performed in an Ar-filled glove box with concentrations of moisture and oxygen below 1.0 ppm. The charge-discharge cycling performance and cyclic voltammetry (0.05-2.5 V, 0.2 mV s^{-1}) was performed at room temperature on an electrochemical workstation (CHI 660 C) at different cycle number with a voltage window of 0.05-2.5 V. The impedance measurements were performed at frequencies ranging from 10^{-2} to 10^5 Hz.

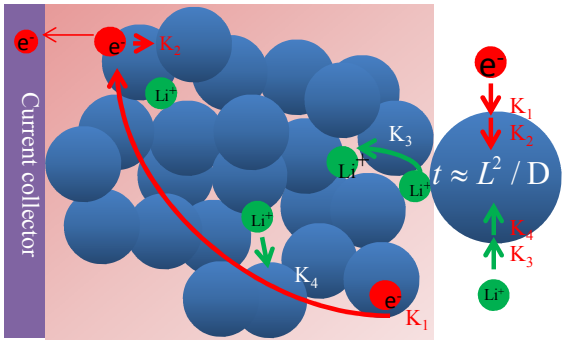

K_1: charge transfer kinetics (electrode surface)
K_2: charge diffusion kinetics (crystal lattice)
K_3: lithium-ion diffusion kinetics (electrolyte)
K_4: lithium-ion diffusion kinetics (crystal lattice)

Scheme 1. Schematic illustration of the transfer and diffusion principle of both charge and lithium ion of the aggregated nanocrystals electrodes.

3. Results and discussion

To understand the crystal phase of C-Bi_2O_3 and A-Bi_2O_3 and the transformation process of BICH precursor, the crystal structures of the three samples A-Bi_2O_3, C-Bi_2O_3 and precursor BICH were characterized by XRD, as shown Fig. 1. From the XRD patterns, we can draw two conclusions. One is the A-Bi_2O_3 is transformed from the decomposition of the precursor BICH. In addition, the crystal phase of A-Bi_2O_3 and C-Bi_2O_3 is identical and both the XRD patterns matched well with JCPDS card no. 71-0465 for monoclinic Bi_2O_3 with a = 5.8496, b = 8.1648 nm and c = 7.5101 nm. The same crystal phase is favourable for the comparison of the electrochemical performance of the two samples since the crystals structure and morphology are two important features for

the LIBs performance. We noted that the crystallinity of C-Bi_2O_3 is better than that of A-Bi_2O_3. Generally speaking, under identical conditions, poor crystallinity will deteriorate the cycling performance of LIBs. However, our experimental results show that the electrochemical properties of A-Bi_2O_3 electrode exhibited superior performance compared to the C-Bi_2O_3 electrode; detail discussion will be described later.

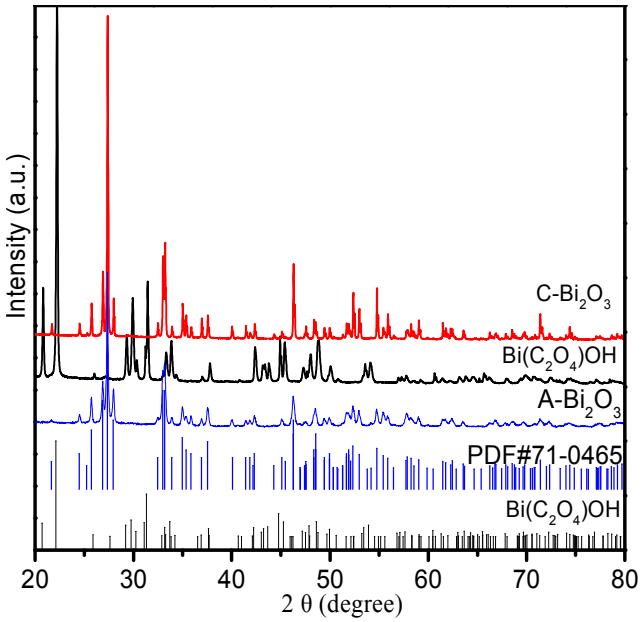

Fig.1 XRD patterns of the precursor BICH, A-Bi_2O_3 and C-Bi_2O_3. The bars are from Bi_2O_3 (JCPDS card no. 71-0465) and precursor BICH.

In addition, the morphology is another important factor for determining the LIBs performance. Currently, various morphologies had been extensively studied for the improvement in LIBs performance.[9, 17, 21, 23] In comparison, the FESEM images of C-Bi_2O_3 and A-Bi_2O_3 at different magnification is presented in Fig. 2. It can be readily observed that the microstructure of C-Bi_2O_3 is randomly microparticles, as shown in Fig. 2 (a)-(c), whereas the obtained A-Bi_2O_3 consists of one-dimensional crystal structure, exhibits a ribbon-like morphology, and has width of 1 to 2 μm, thickness of 200 to 400 nm, and length of 5 to 20 μm, as shown in Fig. 2 (d)-(f). It should be noted that the morphology of A-Bi_2O_3 is well preserved after the thermal decomposition of BICH. To reveal the evolution process of ribbon-like structured materials, the time-dependant experiments were carried out. Interestingly, it was found that the ribbon-like materials are readily formed in the early stage during the hydrothermal process. Moreover, an interesting phenomenon was observed that the dimension of ribbon-like materials is successfully increased with the increase of reaction time, as shown in Fig. S1. Further detailed investigations on the reaction time dependence on the dimension change and the electrochemical behaviour of ribbon-like Bi_2O_3 are currently in progress. In addition, considering the similar morphology, we made a comparison analysis of crystal structures of BICH and Bi_2O_3, as shown in Fig. S2. Interestingly, the arrangement of BiO_6 octahedrons is similar to that of Bi_2O_3.The detailed 1D BICH structure had been well elucidated in previously literature.[29] Compared to BICH, zigzaglike chain connected to BiO_6 octahedrons only occurred a little distorted.

According to the experimental results, the 1D BICH are readily transformed to 1D Bi_2O_3 without the structure change. In addition, the comparison of the crystal structures shown in Tab. S1 means that the phase transformation of BICH from tetragonal phase to monoclinic phase (Bi_2O_3) occurs, moreover, the unit cell volume shrinks obviously during the thermal treatment process. In addition, it is worthwhile to note that significant changes of (*hkl*), for example, there are a shrinkage of the a-axis and b-axis and a significant increase of c-axis. As the unique ribbon-like structure, the increase of c-axis and the decrease of a-axis and b-axis may increase the lithium-ion diffusion coefficient due to the 1D pore channel structure , as shown Fig. S2 and Scheme.2.

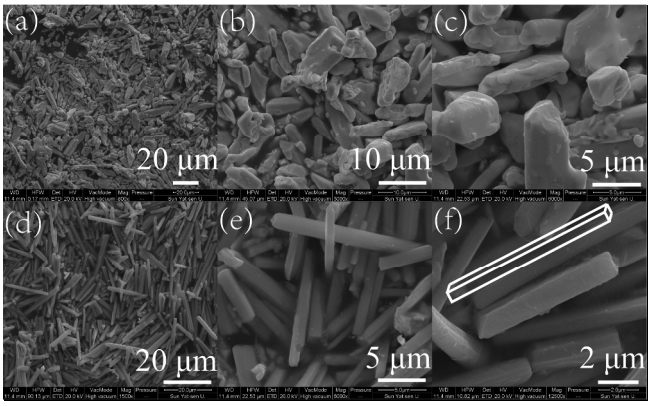

Fig. 2 Typical FESEM images of the C-Bi_2O_3 (a)-(c) and A-Bi_2O_3 (d)-(f) at different magnifications. A schematic image was shown in the inset of Fig. 2 (f).

As shown in Fig. 3, the TG-DTG analysis of the precursor gave a direct evidence of how much temperature is appropriate to obtain Bi_2O_3. From the analysis of TG-DTG curves, about 274 ℃ is the crystal phase transition temperature. Therefore, we select 300 ℃ as the thermal decomposition temperature of the BICH. At high temperature, for example, at 400 ℃ , the ribbon-like structure is severely destroyed, as shown in Fig. S3. Therefore, the appropriate temperature should be optimized to obtain the proper ribbon-like structure.

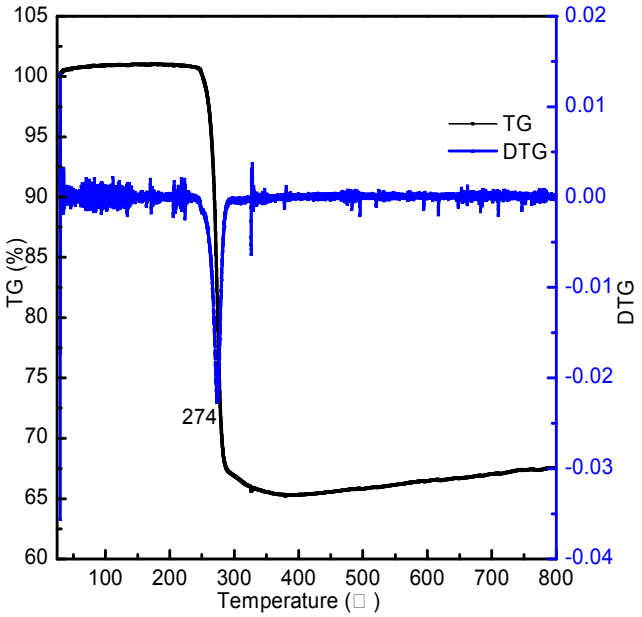

Fig. 3 TG-DTG curve of the BICH precursor. It can decompose completely at about 274 ℃.

To further reveal the microstructure of A-Bi_2O_3, the TEM and HRTEM were carried out, as shown in Fig. 4. Fig. 4a shows an identical morphology presented in Fig. 2 (f). Interestingly, the HRTEM of end of ribbon revealed that amorphous carbon is uniformly coated in the surface of A-Bi_2O_3, which is rather favourable for high-performance LIBs. Currently, the carbon-coating technologies had been widely studied for improving the LIBs performance, to the best of our knowledge and this carbon-coated way had never been reported. Where is thin carbon layer from? It can be reasonably inferred that the carbon layer should be from the decomposition of Bi(C_2H_4)OH during the formation process of Bi_2O_3. Undoubtedly, the technology will provide new route for high-performance LIBs in the future. The clear lattice fringes, parallel to each other, show that the edge of A-Bi_2O_3 is well-crystallized, and the interplanar distance between adjacent lattice planes is 0.325 nm (Fig. 4(c)), corresponding to the d-spacing value of Bi_2O_3 (-121) planes. A. The corresponding SAED is shown in Fig.4 (d), indicating a polycrystal structure of end of microribbons. The existence of white light circle also indicates that existence of the amorphous carbon layer. The stoichiometric composition of the A-Bi_2O_3 with amorphous carbon layer was further confirmed with our EDX analysis (atomic ratio of Bi/O, 2:3, Fig. S4).

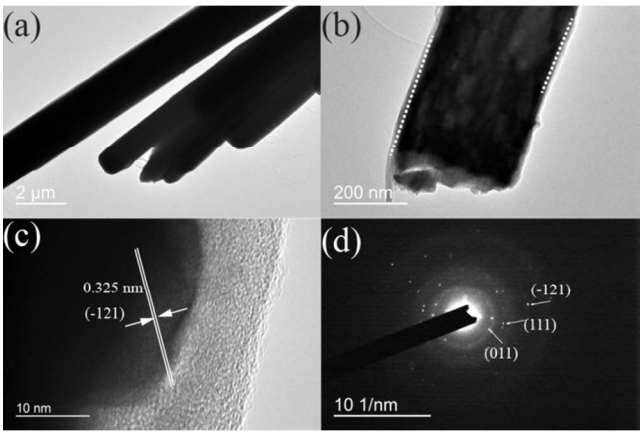

Fig.4 Typical TEM images of the A-Bi_2O_3 (a) low magnification, (b) high magnification, (c) representative HRTEM image of the edge of A-Bi_2O_3 taken along [001] axis and its corresponding SAED (d).

In order to compare the electrochemical properties of the C-Bi_2O_3/Li and A-Bi_2O_3/Li half cells, the cycling performance of the fabricated half cells was carried out. Li-cycling in the voltage of 0.05-2.5 V vs Li at the current rate of 150 mA g^{-1} are shown in Fig. 5(a), (b). For clarify, we selected the 1st, 2nd, 5th and 10th. For C-Bi_2O_3/Li half cell, as indicated, the initial charge-discharge capacities of ~759 mAh g^{-1} and ~1272 mAh g^{-1}, respectively, with a Coulombic efficiency of 59.7 %. In the second cycle, a discharge capacity of 1010 mAh g^{-1} indicated that 20.6 % of the initial discharge capacity is irreversible. This can be attributed to an inactive solid electrolyte interface (SEI) layer on the electrode surface and the decomposition of the electrolyte.[30] The discharge capacities of the 5th and 10th cycles remain large, ~971 and ~943 mAh g^{-1}, respectively, corresponding to the retention of 96.1 % and 93.4 % as compared to the second discharge capacity (1010 mAh g^{-1}). In comparison, the A-Bi_2O_3 has a much higher capacity, for the 1st, 2nd, 5th and 10th , the charge capacities are ~1195, 1176, 1074 and 984 mAh g^{-1}, respectively, whereas the discharge capacities are ~1598, 1470, 1323 and 1304 mAh g^{-1}, respectively. We believe that there are at least two reasons for A-Bi_2O_3 to deliver a significantly enhanced electrochemical performance. First microribbon structure can effectively accommodated the volume change during the charge-discharge process. Secondly, the amorphous carbon layer on the surface of the A-Bi_2O_3, acts a conductive pathway for effective charge transfer. This phenomenon has been observed on other anode materials as well.[7, 31, 32] It should be noted, however, that the Coulombic efficiency of cycling in the current study is consistently low (around 75% for the first 10 cycles), which is much inferior as compared to many other anode materials.[4, 5, 8-10]

We think that the Bi_2O_3 microribbons were not electrochemically active before 10 cycles, which may be due to its unique micrometer and one-dimensional structure characteristics. From the SEI point of view, there may be some changes of the interface between the electrodes surface and the electrolyte. The main reason was currently under progress.

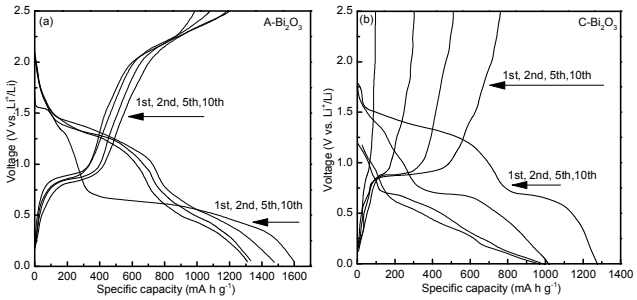

Fig. 5 Charge-discharge profiles of A-Bi_2O_3/Li and C-Bi_2O_3/Li half cells at a constant current density of 150 mA g^{-1}.

Fig. 6 shows the cycling performance of A-Bi_2O_3/Li and C-Bi_2O_3/Li half cells. Compared to C-Bi_2O_3/Li, the A-Bi_2O_3/Li half cell displays superior cycling performance, for which it can deliver stable discharge capacities of ~1047, 849 and 672 mAh g^{-1}, respectively, after 100 cycles at different current density (150, 300, 450 mA g^{-1}) (Fig. 6 (a)), whereas for the C-Bi_2O_3/Li half cell, under the identical conditions, it only deliver discharge capacities of ~853, 615 and 248 mAh g^{-1} (Fig. 6 (b)). The rate performance of C-Bi_2O_3/Li and A-Bi_2O_3/Li half cells is also tested to study the fast discharge behaviour. As shown in Fig. 7, the discharge rates are increased successively from 150 to 750 mA g^{-1} for each 10 cycles. For the A-Bi_2O_3/Li half cell, as shown in Fig. 7 (a), the average discharge capacities for each 10 cycles at 150, 300, 450, and 600 mA g^{-1} are ~1137, 831, 607 and 386 mAh g^{-1}, respectively. At a high rate of 750 mA g^{-1}, it can still deliver a discharge capacity of ~248 mAh g^{-1}. When the rate is decreased back to 150 mA g^{-1}, 80% discharge capacity of the initial 10 cycles at 150 mA g^{-1} has been recovered, indicating a superior rate capability. Obviously, the A-Bi_2O_3/Li half cell exhibits a superior rate performance in comparison with C-Bi_2O_3/Li half cell (Fig. 7 (b)). Moreover, the morphology of A-Bi_2O_3 can be well preserved during lithium intercalation/deintercalation process even under the current density of 450 mA g^{-1} for 100 cycles (Fig. 8), which are helpful in improving the electrochemical performance of the electrode. The superior rate capability exhibited by A-Bi_2O_3 suggests them as promising anode material for lithium ion battery with large power densities.

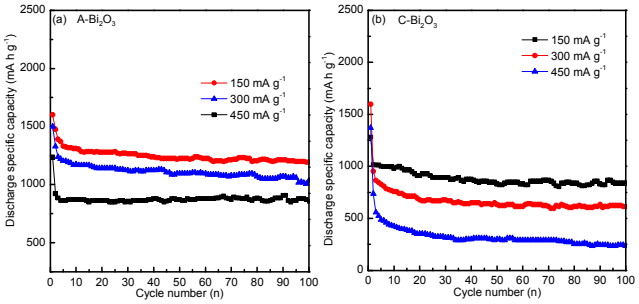

Fig. 6 The cycle performance of A-Bi_2O_3/Li half cells. (a) and C-Bi_2O_3/Li (b) at different current density.

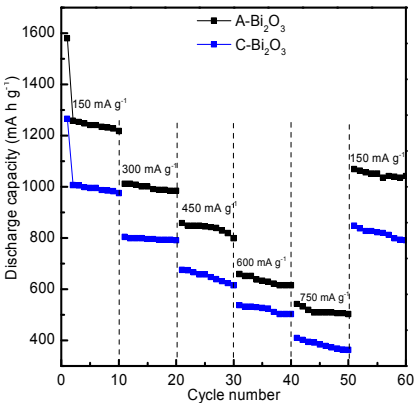

Fig. 7 Rate performance of A-Bi_2O_3/Li and C-Bi_2O_3/Li half cells.

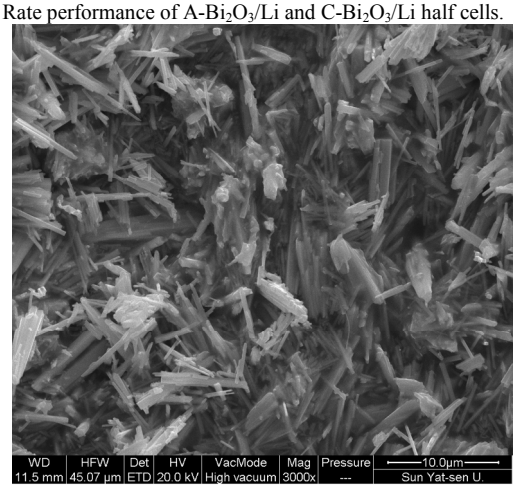

Fig. 8 FESEM image of the Bi_2O_3 microribbons after 100 cycles of charge and discharge process under the current density of 450 mA g^{-1}.

The electrochemical behavior of A-Bi_2O_3/Li half cell is characterized by cyclic voltammetry (CV) at the scanning rate of 0.2 mV s^{-1} between 0.05 and 3.5 V, as shown in Fig. 9. Fig. 9 shows CV curves of the A-Bi_2O_3 and C-Bi_2O_3 electrodes, respectively, both first three cycles. On the basis of the CVs, the lithium insertion and extraction reactions for A-Bi_2O_3/Li half cell are believed to proceed as follows:

$$Bi_2O_3 + 6Li^+ + 6e^- \longrightarrow 2Bi + 3Li_2O \quad (1)$$

$$Bi_2O_{2.33} + 4.66\,Li^+ + 4.66e^- \longrightarrow 2Bi + 2.33Li_2O \quad (2)$$

$$Bi + Li^+ + e^- \longrightarrow LiBi \quad (3)$$

$$LiBi + 2Li^+ + 2e^- \longrightarrow Li_3Bi \quad (4)$$

$$Li_3Bi \longrightarrow Bi + 3Li^+ + 3e^- \quad (5)$$

$$2Bi + 3Li_2O \longrightarrow Bi_2O_3 + 6Li^+ + 6e^- \quad (6)$$

For A-Bi_2O_3/Li half cell, each peak position shown in Fig. 9 (a) is analyzed as follows. Anodic peak of 0.44 V corresponds the alloying reaction of Bi and Li, and the formation of SEI layer.[33] During the subsequent cycle, namely, the 2nd cycle, the peak is replaced by other two minor peaks, 0.75 V and 0.64 V, indicating the formation of LiBi and Li_3Bi, which correspond to the electrochemical lithium insertion reaction of eqn (3) and (4), respectively. The cathodic peak of 1.24 V is associated with the reduction of Bi_2O_3 to metal Bi (eqn 1) while the peak at 1.45 V may correspond to reduction of tetragonal $Bi_2O_{2.33}$ (eqn 2).[34] The small anodic peaks of 2.24 V and 1.77 V are associated with the oxidation of Bi to Bi_2O_3, which correspond to eqn (6). The

obvious anodic peak at 0.97 V is associated with the de-alloying process. For comparison, the C-Bi_2O_3/Li half cell was also evaluated under identical conditions. In comparison with the C-Bi_2O_3 electrode (Fig. 9 (b)), the A-Bi_2O_3 electrode exhibits sharper peak and higher current intensity, suggesting that good kinetic behaviors of both lithium ion diffusion and charge transfer of A-Bi_2O_3 electrode during the charge-discharge process.

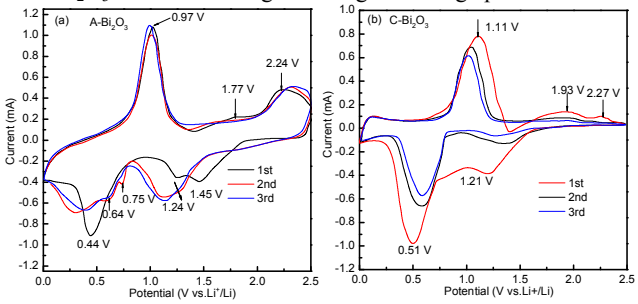

Fig. 9 Cyclic voltammetry for the first three cycles of A-Bi_2O_3/Li half cell (a) and C-Bi_2O_3/Li half cell (b) at scan rate of 0.2 mV s^{-1}.

Electrochemical impedance spectroscopy (EIS) measurements are carried out in order to evaluate the electrode kinetic behaviour of as-prepared C-Bi_2O_3/Li and A-Bi_2O_3/Li half cells. The impedance measurements are performed after charge-discharge for 5 cycles at a discharge potential of 0.75 V vs. Li/Li^+. The Nyquist plots of the two electrodes are shown in Fig. 10. Both of the fresh cells display a high charge-transfer resistance. It can be seen clearly that the R_{ct} is much smaller for the A-Bi_2O_3/Li half cell (about 297 Ω) electrode than for the C-Bi_2O_3/Li half cell (about 212 Ω) electrode after the 5th cycle, which indicates that the ribbon structure could enable faster charge transfer at the electrode/electrolyte interface and favor in reducing electrode polarization and therefore, decrease the overall LIBs internal resistance. Moreover, the ribbon-like structure can also lead to better accommodation of the strain and change of volume change induced during charge-discharge process, which is favour for the cycle life of LIBs, which had been demonstrated in other ribbon-like anode materials. [24, 26] In addition, the amorphous carbon coating significantly enhances the conductivity of the A-Bi_2O_3 material, since the conductive amorphous coating layer facilitates electronic conductive paths in the A-Bi_2O_3 belts, which is considered a key factor in improving the performance of LIBs, in particular, the charge-discharge capacity and rate capability of the A-Bi_2O_3/Li half cell. The following factors can account for this result: (1) the ribbon structure and open spaces can not only provide more sites for the adsorption of lithium ions, but also facilitate the fast their intercalation and deintercalation of active species; (2) the conductive layer of amorphous carbon directly formed on the surface of the A-Bi_2O_3 is favorable for electron collection and transfer (Scheme 1). Therefore, the A-Bi_2O_3 exhibited superior rate and cycling performance.

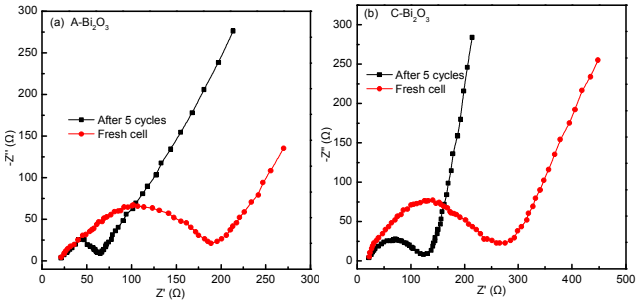

Fig.10 Nyquist plots of Bi_2O_3/Li cells. (a) A-Bi_2O_3/Li half cell, (b) C-Bi_2O_3/Li half cell at the 0.75 V during the 5th discharge.

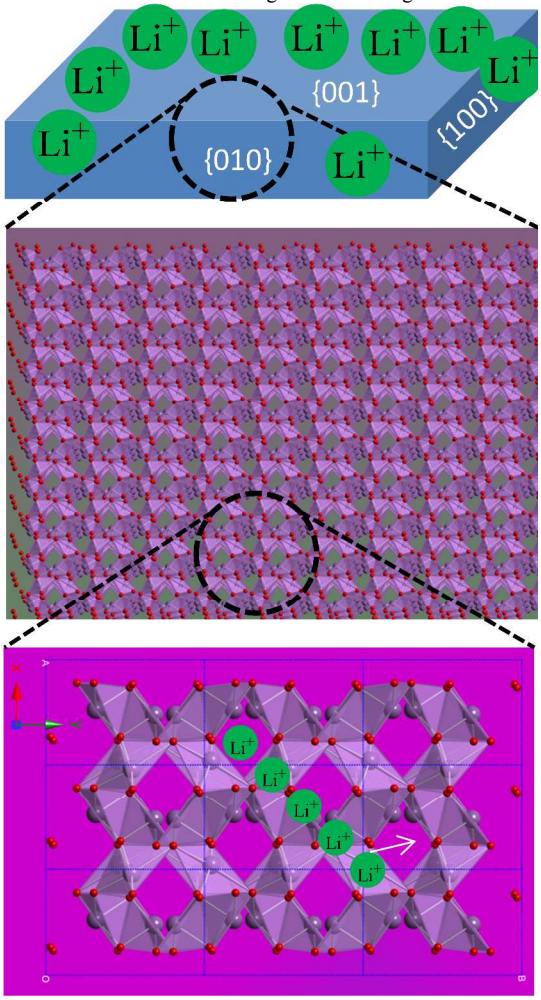

Scheme 2 Simple schematic representations of Li-ion diffusion paths in A-Bi_2O_3 microribbons.

4. Conclusions

In summary, we have synthesized Bi_2O_3 microribbons through facile thermal decomposition and morphologically conserved transformation of $Bi(C_2O_4)OH$ synthesized by topochemical synthesis. It was found that the amorphous carbon was uniformally coated on the surface of the Bi_2O_3 microribbons without extra carbon-coated process. We have further investigated the prospect of using the carbon-coating microribbons as an anode for LIBs and demonstrated high reversible capacity and good cyclability. The enhanced electrochemical performance can be attributed to the synergistic

effects of the carbon layer and microribbon structure. The experimental results further demonstrated that the microribbon is an effective structure for high-performance LIBs. This work provides new opportunities for the development of high-performance anode materials for LIBs.

Acknowledgements

We gratefully acknowledge financial support from National Natural Science Foundation of China (No. 41272064), Department of Education, Guangxi Zhuang Autonomous Region of China (Nos. 200103YB061 and 201010LX188) and PolyU's Postdoctoral Dean Reserve Project (1-ZV9F).

Notes and references

Renewable Energy Research Group (RERG), Department of Building Services Engineering, The Hong Kong Polytechnic University, Room: ZN816, Kowloon, Hong Kong, China. Fax: +852-27746146; Tel: +852-27665863; E-mail: bxhxyang@polyu.edu.hk.

† Electronic Supplementary Information (ESI) available: [details of any supplementary information available should be included here]. See DOI: 10.1039/b000000x/

‡ Footnotes should appear here. These might include comments relevant to but not central to the matter under discussion, limited experimental and spectral data, and crystallographic data.

1 B. L. Ellis, K. T. Lee and L. F. Nazar, *Chem. Mater.*, 2010, **22**, 691-714.
2 J. B. Goodenough and Y. Kim, *Chem. Mater.*, 2010, **22**, 587-603.
3 Y. G. Li, B. Tan and Y. Y. Wu, *Nano Lett.*, 2008, **8**, 265-270.
4 G. F. Xia, N. Li, D. Y. Li, R. Q. Liu, N. Xiao and D. Tian, *Mater. Lett.*, 2011, **65**, 3377-3379.
5 J. Y. Shen, H. Wang, Y. Zhou, N. Q. Ye, G. B. Li and L. J. Wang, *RSC Adv.*, 2012, **2**, 9173-9178.
6 W. Tang, X. W. Gao, Y. S. Zhu, Y. B. Yue, Y. Shi, Y. P. Wu and K. Zhu, *J. Mater. Chem.*, 2012, **22**, 20143-20145.
7 J. W. Zhang, X. X. Yan, J. W. Zhang, W. Cai, Z. S. Wu and Z. J. Zhang, *J. Power Sources*, 2012, **198**, 223-228.
8 J. M. Ma, J. Zhang, S. R. Wang, Q. H. Wang, L. F. Jiao, J. Q. Yang, X. C. Duan, Z. F. Liu, J. B. Lian and W. J. Zheng, *CrystEngComm*, 2011, **13**, 6077-6081.
9 J. Y. Shen, H. Wang, Y. Zhou, N. Q. Ye and L. J. Wang, *CrystEngComm*, 2012, **14**, 6215-6220.
10 X. M. Wu, S. C. Zhang, L. L. Wang, Z. J. Du, H. Fang, Y. H. Ling and Z. H. Huang, *J. Mater. Chem.*, 2012, **22**, 11151-11158.
11 M. Wachtler, J. O. Besenhard and M. Winter, *J. Power Sources*, 2001, **94**, 189-193.
12 K. T. Lee, Y. S. Jung and S. M. Oh, *J. Am. Chem. Soc.*, 2003, **125**, 5652-5653.
13 J. W. Deng, H. X. Ji, C. L. Yan, J. X. Zhang, W. P. Si, S. Baunack, S. Oswald, Y. F. Mei and O. G. Schmidt, *Angew. Chem. Int. Ed.*, 2013, **52**, 2326-2330.
14 J. H. Kong, W. A. Yee, Y. F. Wei, L. P. Yang, J. M. Ang, S. L. Phua, S. Y. Wong, R. Zhou, Y. L. Dong, X. Li and X. H. Lu, *Nanoscale*, 2013, **5**, 2967-2973.
15 A. Finke, P. Poizot, C. Guery, L. Dupont, P. L. Taberna, P. Simon and J. M. Tarascon, *Electrochem. Solid-State Lett.*, 2008, **11**, E5-E9.
16 C. M. Park, S. Yoon, S. I. Lee and H. J. Sohn, *J. Power Sources*, 2009, **186**, 206-210.
17 J. M. Ma, J. Q. Yang, L. F. Jiao, T. H. Wang, J. B. A. Lian, X. C. Duan and W. J. Zheng, *Dalton Trans.*, 2011, **40**, 10100-10108.
18 Y. L. Li, M. A. Trujillo, E. G. Fu, B. Patterson, L. Fei, Y. Xu, S. G. Deng, S. Smirnov and H. M. Luo, *J. Mater. Chem. A*, 2013, **1**, 12123-12127.
19 J. Y. Shen, H. Wang, Y. Zhou, N. Q. Ye, Y. H. Wang and L. J. Wang, *Chem. Eng. J.*, 2013, **228**, 724-730.
20 Q. S. Gao, L. C. Yang, X. C. Lu, J. J. Mao, Y. H. Zhang, Y. P. Wu and Y. Tang, *J. Mater. Chem.*, 2010, **20**, 2807-2812.
21 E. Hosono, T. Kudo, I. Honma, H. Matsuda and H. S. Zhou, *Nano Lett.*, 2009, **9**, 1045-1051.
22 J. Y. Liao, D. Higgins, G. Lui, V. Chabot, X. C. Xiao and Z. W. Chen, *Nano Lett.*, 2013, **13**, 5467-5473.
23 L. Q. Mai, F. Yang, Y. L. Zhao, X. Xu, L. Xu and Y. Z. Luo, *Nat. Commun.*, 2011, **2**.
24 J. S. Chen, Y. L. Cheah, S. Madhavi and X. W. Lou, *J. Phys. Chem. C*, 2010, **114**, 8675-8678.
25 Y. X. Sun, J. Wang, B. T. Zhao, R. Cai, R. Ran and Z. P. Shao, *J. Mater. Chem. A*, 2013, **1**, 4736-4746.
26 X. Y. Xue, Z. H. Chen, L. L. Xing, S. Yuan and Y. J. Chen, *Chem. Commun.*, 2011, **47**, 5205-5207.
27 J. L. Hu, H. M. Li, C. J. Huang, M. Liu and X. Q. Qiu, *Appl.Cata. B: Enviro.*, 2013, **142**, 598-603.
28 B. Ling, X. W. Sun, J. L. Zhao, Y. Q. Shen, Z. L. Dong, L. D. Sun, S. F. Li and S. Zhang, *J. Nanosci. Nanotechnol.*, 2010, **10**, 8322-8327.
29 M. Rivenet, P. Roussel and F. Abraham, *J. Solid State Chem.*, 2008, **181**, 2586-2590.
30 Y. Z. Su, S. Li, D. Q. Wu, F. Zhang, H. W. Liang, P. F. Gao, C. Cheng and X. L. Feng, *ACS Nano*, 2012, **6**, 8349-8356.
31 J. Q. Zhao, J. P. He, J. H. Zhou, Y. X. Guo, T. Wang, S. C. Wu, X. C. Ding, R. M. Huang and H. R. Xue, *J. Phys. Chem. C*, 2011, **115**, 2888-2894.
32 J. Zhu, D. N. Lei, G. H. Zhang, Q. H. Li, B. G. Lu and T. H. Wang, *Nanoscale*, 2013, **5**, 5499-5505.
33 J. C. Perez-Flores, A. Kuhn and F. Garcia-Alvarado, *J. Power Sources*, 2008, **182**, 365-369.
34 G. Pistoia, M. Pasquali and F. Rodante, *J. Power Sources*, 1985, **16**, 263-269.